Effect of polymer-stress diffusion in the numerical simulation of elastic turbulence

Anupam Gupta[1] and Dario Vincenzi[2]†

[1]Paulson School of Engineering and Applied Sciences, Harvard University, Cambridge, Massachusetts 02138, USA

[2]Université Côte d'Azur, CNRS, LJAD, 06100 Nice, France

Elastic turbulence is a chaotic regime that emerges in polymer solutions at low Reynolds numbers. A common way to ensure stability in numerical simulations of polymer solutions is to add artificially large polymer-stress diffusion. In order to assess the accuracy of this approach in the elastic-turbulence regime, we compare numerical simulations of the two-dimensional Oldroyd-B and FENE-P models sustained by a cellular force with and without artificial diffusion. We find that artificial diffusion can have a dramatic effect even on the large-scale properties of the flow and we show some of the spurious phenomena that may arise when artificial diffusion is used.

1. Introduction

Polymer solutions can exhibit a chaotic behaviour, even at low Reynolds numbers, as a result of purely elastic instabilities (Groisman & Steinberg 2000, 2004). This regime of polymer solutions, known as elastic turbulence, finds a natural application in microfluidics, where the typical Reynolds numbers are very low and the addition of polymers to the fluid can be employed to accelerate phenomena such as mixing (Groisman & Steinberg 2001), emulsification (Poole *et al.* 2012) and heat transfer (Traore, Castelain & Burghelea 2015; Abed *et al.* 2016) or to examine the dynamics of microscopic objects in fluctuating flows (Liu & Steinberg 2014).

The numerical simulation of elastic turbulence is challenging for at least three reasons. The first two are common to the high-Reynolds-number regime of polymer solutions. Indeed, the available constitutive models of viscoelastic fluids are based on rather crude approximations and disregard several, potentially relevant aspects of polymer dynamics (Bird *et al.* 1987). In addition, a high spatial resolution and advanced numerical schemes are needed to resolve the sharp gradients that form in the polymer-stress field (Jin & Collins 2007; Plan *et al.* 2017). The third reason is specific to elastic turbulence and is the requirement that the time step used for the integration of the Navier–Stokes equations be small; this requirement is a consequence of the high viscosity of the fluid (Press *et al.* 2007).

Most numerical studies of elastic turbulence have therefore considered simplified flow configurations (e.g. in two dimensions and/or with periodic boundary conditions) and have been restricted to limited ranges of parameters. Notwithstanding, even simple models of viscoelastic fluids in idealized settings have proved successful in capturing the main properties of elastic turbulence. Several experimental observations are reproduced, at least qualitatively, by the Oldroyd-B model, in which only the slowest oscillation mode

† Email address for correspondence: dario.vincenzi@unice.fr

of the polymer is retained and polymer elasticity is assumed to be linear (Berti *et al.* 2008; Thomases & Shelley 2009; Berti & Boffetta 2010; Thomases, Shelley & Thiffeault 2011; Grilli, Vázquez-Quesada & Ellero 2013; Plan *et al.* 2017; van Buel, Schaaf & Stark 2018; Garg *et al.* 2018). Other studies have used the FENE-P model, which improves on the Oldroyd-B one by taking into account the finite extensibility of polymers (Liu & Khomami 2013; Gupta & Pandit 2017), or have taken a Lagrangian approach and have solved the dynamics of a large number of dumbbell-like polymers (Watanabe & Gotoh 2013, 2014). In fact, even a low-dimensional 'shell model' of viscoelastic fluid reproduces elastic turbulence qualitatively (Ray & Vincenzi 2016).

Constitutive models such as the Oldroyd-B and the FENE-P ones consist of a coupled system of partial differential equations for the velocity of the solution and for the polymer stress tensor. This latter is by nature positive definite, but numerical errors may lead to the loss of this property and hence to instabilities (Joseph 1990). A standard way to prevent such instabilities is to include *global* artificial diffusivity in the model, i.e. to add a Laplacian term to the evolution equation for the polymer stress with a space-independent coefficient (Sureshkumar & Beris 1995). Numerical simulations of turbulent polymer solutions that use artificial diffusivity are in qualitative agreement with experiments (e.g. Graham 2014, and references therein). Polymer-stress diffusion in fact has a physical origin, for it results from the diffusion of the centre of mass of polymers due to thermal noise (El-Kareh & Leal 1989). However, the values of diffusivity needed to achieve numerical stability are three to six orders of magnitude greater than those appropriate for real polymers (e.g. Vaithianathan *et al.* 2006). For this reason, numerical schemes have been proposed that avoid using artificial diffusivity. These include, inter alia, schemes that only employ polymer diffusivity at those locations in the fluid where the polymer stress loses its positive definite character (Min, Yoo & Choi 2001), methods adapted from hyperbolic solvers (Vaithianathan *et al.* 2006), or schemes based on representations of the polymer stress tensor that guarantee the preservation of its positive definiteness (Vaithianathan & Collins 2003; Fattal & Kupferman 2003; Balci *et al.* 2011; Hameduddin *et al.* 2018). Such numerical schemes have been compared with simulations using artificial diffusivity at high or moderate Reynolds numbers, and quantitative discrepancies have emerged: for instance, the level of drag reduction is diminished by artificial diffusivity, the velocity and polymer-stress fields are significantly smeared, excessive polymer-stress diffusion leads to relaminarization (Min *et al.* 2001; Vaithianathan *et al.* 2006; Sid, Terrapon & Dubief 2018). Thus a consensus seems to have formed that at high or moderate Reynolds numbers alternative methods should be preferred to the use of artificial diffusivity.

At low Reynolds numbers, several studies on elastic turbulence have employed artificial diffusivity (Berti *et al.* 2008; Thomases & Shelley 2009; Berti & Boffetta 2010; Thomases *et al.* 2011; Liu & Khomami 2013; Garg *et al.* 2018). It was shown in Thomases (2011) that in viscoelastic creeping flows this has the effect of smoothing the polymer-stress field and keeping it bounded. However, to the best of our knowledge, the effect of artificial diffusivity in the elastic-turbulence regime has not been examined yet. This is the object of the present study, in which we compare numerical simulations with and without artificial diffusivity. As a case study, we consider the Oldroyd-B model with a cellular forcing on a periodic square (analogous simulations of the FENE-P model are presented in the Appendix). The cellular forcing generates distinct regions of straining and vorticity and thus allows us to describe a flow configuration in which the effect of artificial diffusivity is particularly adverse. Our results demonstrate that the properties of the velocity field are strongly affected, to such an extent that also the large-scale flow may be misrepresented. In particular, we show that some phenomena observed

in previous simulations are due to artificial stress diffusion and are not present when alternative integration methods are used.

The general effect of artificial diffusivity is to spread high polymer stresses over large regions of the flow, including those where the polymer stress would be weak because vorticity dominates and polymers should not be stretched. We shall se that, in elastic turbulence, this fact leads to a spurious symmetry breaking analogous to that observed in Thomases & Shelley (2009) and Thomases *et al.* (2011). Indeed, in low-strain regions polymers are weakly stretched and the external force would naturally impose its spatial structure, but if high polymer stresses artificially diffuse into those regions, they prevail over the force and provoke a strong modification of the large-scale flow. This dynamics is specific to elastic turbulence, because the Reynolds number is low and, in the absence of artificial diffusivity, the original laminar flow is weakly perturbed by the addition of polymers in vorticity-dominated regions. At high Reynolds numbers the effect of artificial diffusivity is less dramatic, since the flow is already chaotic before the addition of polymers and therefore artificial diffusivity does not change the large-scale flow so strongly. Indeed, at high Reynolds numbers, the differences between simulations with and without artificial diffusivity are essentially quantitative (Vaithianathan *et al.* 2006; Sid *et al.* 2018). In conclusions, we show that in elastic turbulence artificial diffusivity induces dramatic qualitative modifications of the large-scale flow, which are not observed at high Reynolds numbers. Hence the study of the low-Reynolds-number regime requires a separate study.

2. Viscoelastic model

The Oldroyd-B model (Oldroyd 1950) describes the deformation of polymers by means of a space-time dependent positive-definite tensor: the polymer conformation tensor $\boldsymbol{C}(\boldsymbol{x}, t)$. In the limit of vanishing inertia, the coupled evolution of $\boldsymbol{C}(\boldsymbol{x}, t)$ and the velocity field $\boldsymbol{u}(\boldsymbol{x}, t)$ that describes the motion of the solution is given by the following equations:

$$\boldsymbol{\nabla} p = \nu \Delta \boldsymbol{u} + \frac{\mu}{\tau} \boldsymbol{\nabla} \cdot \boldsymbol{C} + \boldsymbol{f}, \qquad \boldsymbol{\nabla} \cdot \boldsymbol{u} = 0, \tag{2.1a}$$

$$\partial_t \boldsymbol{C} + \boldsymbol{u} \cdot \boldsymbol{\nabla} \boldsymbol{C} = (\boldsymbol{\nabla} \boldsymbol{u}) \cdot \boldsymbol{C} + \boldsymbol{C} \cdot \boldsymbol{\nabla} \boldsymbol{u})^\top - \frac{1}{\tau} (\boldsymbol{C} - \boldsymbol{I}), \tag{2.1b}$$

where p is pressure, ν is the kinematic viscosity of the solvent, τ is the polymer relaxation time, the components of the velocity gradient are defined as $(\boldsymbol{\nabla} \boldsymbol{u})_{ij} = \partial u_i / \partial x_j$ and $\boldsymbol{I}$ is the identity matrix. The coupling coefficient μ represents the polymer contribution to the total kinematic viscosity of the solution and is proportional to the concentration of polymers. The body force $\boldsymbol{f}(\boldsymbol{x})$ that sustains the motion of the solution is such that $\boldsymbol{\nabla} \cdot \boldsymbol{f} = 0$. In the above equations, the conformation tensor is rescaled with the polymer mean square equilibrium extension in the absence of flow.

In considering the limit of the Oldroyd-B model for vanishing inertia, we follow Fouxon & Lebedev (2003); Thomases & Shelley (2009); Thomases *et al.* (2011); Balci *et al.* (2011), who describe the motion of the solution by means of the Stokes equations in lieu of the Navier–Stokes equations. However, as is discussed in § 4, our conclusions on the effect of artificial diffusivity are unchanged if we use the Navier–Stokes equations with a Reynolds number smaller than the critical value for the appearance of inertial instabilities.

Equations (2.1) are studied on the two-dimensional domain $V = [0, 2\pi]^2$ with periodic boundary conditions. We consider the cellular force:

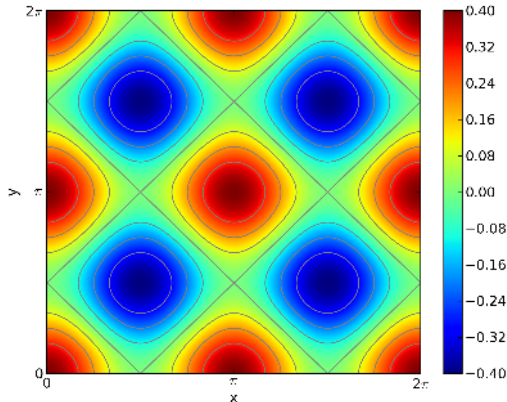$$\boldsymbol{f}(\boldsymbol{x}) = f_0(-\sin Ky, \sin Kx), \tag{2.2}$$

Fig. 1. Vorticity field of the laminar solution of (2.1a) in the absence of polymer feedback, $\omega(\boldsymbol{x}) = -f_0(\cos Kx + \cos Ky)/\nu K$, for $K = 2$, $f_0 = 0.02$ and $\nu = 0.05$.

where f_0 is the amplitude and K the spatial frequency. Cellular-like forcings have been widely used in experiments of chaotic mixing in two-dimensional flows (e.g. Cardoso, Marteau & Tabeling 1994; Rothstein, Henry & Gollub 1999). As is discussed in the conclusions, the effect of artificial diffusivity for other forcings may not be equally dramatic; however, the cellular forcing allows us to clearly identify the fashion in which artificial diffusivity operates in elastic turbulence and to demonstrate how strong its effect can be in this regime.

In the absence of polymer feedback on the flow (i.e. $\mu = 0$), (2.1a) admits the fixed-point laminar solution: $\boldsymbol{u} = -\boldsymbol{f}/\nu K^2$. The corresponding vorticity field $\omega(\boldsymbol{x}, t)$, where $\omega\hat{\boldsymbol{z}} \equiv \boldsymbol{\nabla} \times \boldsymbol{u}$, is shown in figure 1 and consists of a sequence of vortices of alternate sign separated by lines of pure strain. At time $t = 0$, $\boldsymbol{u}$ is the fixed-point velocity field and $\boldsymbol{C}$ is a perturbation of the identity matrix (we use the same perturbation as in Thomases & Shelley 2009, see their equation (3)). By using the length scale $1/K$ and the amplitude $f_0/\nu K^2$ of the laminar velocity, we obtain the turnover time $T = \nu K/f_0$. This allows us to define the Deborah number $De \equiv \tau/T$, which quantifies the ability of the flow to deform polymers.

The reason for choosing the cellular force is twofold. On the one hand, it generates a flow structure in which the straining and vortical regions are clearly separated, similarly to the four-roll mill force considered in Thomases & Shelley (2009) and Thomases $et\ al.$ (2011)—this feature will turn out useful in highlighting the effect of artificial diffusivity on elastic turbulence. On the other hand, the polymer stress generated by the cellular force is less strong than in the case of the four-roll mill force; thus even in the absence of artificial diffusivity a moderate spatial resolution is sufficient to compute the velocity and polymer-stress fields accurately.

In order to preserve the positive definiteness of the conformation tensor, we decompose $\boldsymbol{C}$ according to Cholesky, i.e. we write $\boldsymbol{C} = \boldsymbol{L}\boldsymbol{L}^\top$, where $\boldsymbol{L}$ is a lower triangular matrix and the diagonal elements L_{ii} represent the eigenvalues of $\boldsymbol{C}$. The positivity of $\boldsymbol{C}$ is then ensured by evolving $\ln L_{ii}$ instead of L_{ii} (Vaithianathan & Collins 2003; Perlekar, Mitra, Pandit 2006). The evolution equations for $\ln L_{ii}$ and L_{ij} if $i \neq j$ (see Gupta, Perlekar & Pandit 2015) are solved on a regular grid with 1024^2 collocation points by using a fourth-order finite difference scheme for the spatial derivatives and a fourth-order Runge–Kutta scheme with time step $dt = 2 \times 10^{-3}$ for the temporal integration. The advection terms are treated according to the Kurganov–Tadmor hyperbolic solver (Kurganov & Tadmor

2000). This solver was first applied to the numerical simulation of polymer solutions by Vaithianathan *et al.* (2006). At locations where the original finite-difference scheme would yield a too large gradient of L_{ij} or $\ln L_{ii}$, it selects a lower-order scheme that reduces the gradient. Numerical schemes based on the Kurganov–Tadmor solver have been employed in studies of both turbulent polymer solutions (e.g. Vaithianathan *et al.* 2007; Perlekar, Mitra, Pandit 2010; Dallas, Vassilicos & Hewitt 2010; Robert *et al.* 2010; Valente, da Silva & Pinho 2014; Gupta *et al.* 2015; Shekar *et al.* 2018) and elastic turbulence (Gupta & Pandit 2017; Plan *et al.* 2017). Finally, the velocity field is obtained by solving the vorticity equation associated with (2.1a) in Fourier space.

In order to assess the effect of artificial diffusivity, we also performed simulations which still use the Cholesky decomposition and the Kurganov–Tadmor scheme as described above, but in which we add the term $\kappa\Delta\boldsymbol{C}$ to the right hand side of (2.1b) (or rather the corresponding diffusion terms to the equations for $\ln L_{ii}$ and L_{ij}). We set $\kappa = 5 \times 10^{-5}$, so that the Schmidt number $Sc \equiv \nu/\kappa = 10^3$ is the same as in previous numerical simulations of elastic turbulence (Thomases & Shelley 2009; Thomases *et al.* 2011; Garg *et al.* 2018). This value of Sc is much higher than that used in high-Reynolds-number simulations, where typically $Sc = 0.5$ (e.g. Graham 2014), but is nevertheless three orders of magnitude smaller than it would be in reality (Vaithianathan *et al.* 2006). However, it is not interesting to consider values of Sc much greater than 10^3, because alone they are in general not sufficient to prevent numerical instabilities.

The parameters of the simulations are $K = 2$, $f_0 = 0.02$, $\mu = 0.01$, $\nu = 0.05$, $\tau = 50$ and yield a Deborah number $De = 10$. In particular, the ratio μ/ν is comparable to that used in previous simulations of elastic turbulence. Additional simulations with a different choice of parameters are reported in the online supplementary material and support the results presented in the following section.

3. Results

In this section, we compare numerical simulations of (2.1) based on the two approaches described in § 2, i.e. using either artificial diffusivity with $Sc = 10^3$ or the Kurganov–Tadmor scheme, for which $Sc = \infty$. As we shall see, the effect of artificial diffusivity is so big that to describe it, it is sufficient to examine the qualitative properties of the flow.

Figure 2 shows the time series of the kinetic energy $e(t) \equiv \frac{1}{2} \int_V |\boldsymbol{u}(\boldsymbol{x}, t)|^2 \mathrm{d}\boldsymbol{x}$. For $Sc = 10^3$, the system remains in an almost frozen state for a long time, after which it becomes chaotic. If the simulation is not long enough, such an initial frozen state may lead to a wrong interpretation of the dynamics, since the flow regime may be erroneously described as laminar. The behaviour of $e(t)$ is analogous to that found in Thomases & Shelley (2009) and Thomases *et al.* (2011) for a four-roll mill force and same value of Sc. For $Sc = \infty$, in contrast, the motion of the solution becomes chaotic much more rapidly and, in the steady state, the kinetic energy fluctuates at a frequency much higher than when artificial diffusivity is present. Moreover, the mean kinetic energy is greater.

The time series of the trace of $\boldsymbol{C}$ averaged over V show behaviours analogous to those of $e(t)$, with $\langle \mathrm{tr}\,\boldsymbol{C}\rangle_V$ displaying much slower oscillations when $Sc = 10^3$ and this only after a long, initial, almost frozen state (figure 3).

The snaphots of the vorticity field also indicate a striking difference between the two integration methods (figures 4 and 5). With artificial diffusivity, once the system starts fluctuating the spatial structure of the flow departs from that which would be imposed by the force (figure 4). Only some of the vortical cells continue to exist, whilst others break down and patches of vorticity contaminate the cellular structure of the base flow. Furthermore, the number and the location of unbroken vortical cells vary in time (see the
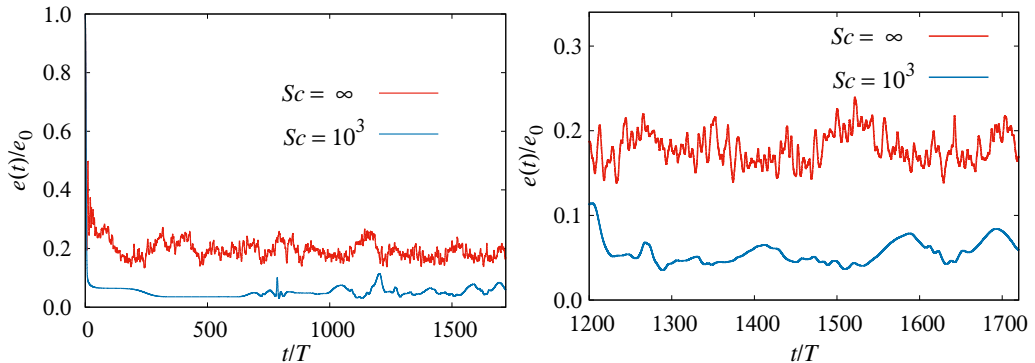
Fig. 2. Left: Time series of the kinetic energy of the polymer solution rescaled by the kinetic energy of the fixed-point laminar flow ($\mu = 0$), i.e. $e_0 \equiv f_0^2/2\nu^2 K^4$, for $Sc = \infty$ (red, top curve) and for $Sc = 10^3$ (blue, bottom curve). Right: zoom of the left panel in the steady state.
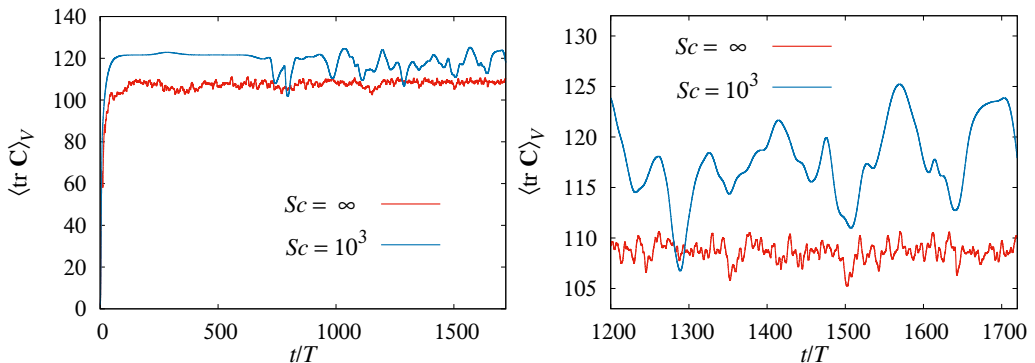

Fig. 3. Left: Time series of the trace of the polymer conformation tensor averaged over the spatial domain V for $Sc = 10^3$ (blue, top curve) and $Sc = \infty$ (red, bottom curve). Right: zoom of the left panel in the steady state.

snapshots at two different times in figure 4). This dynamics is equivalent to the symmetry-breaking transition observed by Thomases & Shelley (2009) and Thomases *et al.* (2011). Contrastingly, for $Sc = \infty$ the vorticity field displays fluctuations which perturb the cellular vortices, but its large-scale structure essentially remains slaved to that of the background force (see figure 5 for a representative snapshot). Large perturbations of the vorticity field are concentrated on thin filaments located in the vicinity of the lines of pure strain which separate the vortical cells. Thus, the symmetry breaking shown in figure 4 is a spurious effect due to artificial diffusivity.

The snapshots of tr $\boldsymbol{C}$ also show a strong qualitative difference in the behaviour of the polymer stress (figures 6). The analysis of these snapshots allows us to understand the effect of artificial diffusivity. Rather than the Schmidt number, here the relevant dimensionless parameter is the Péclet number $Pe = f_0/\kappa\nu K^3$, which is the ratio of the time scale associated with polymer-stress diffusion, $(\kappa K^2)^{-1}$, and the time scale at which the polymer stress is convected, T. When $Sc = \infty$, Pe is also infinite and the evolution of the polymer stress is dominated by convection. In this case, highly-stretched polymers—and hence large polymer stresses—are essentially found in strain-dominated regions of the flow, while the polymer stress is weak in vortical regions, where polymers rapidly contract. Thus, in the cellular flow, the vorticity field is strongly affected by polymer
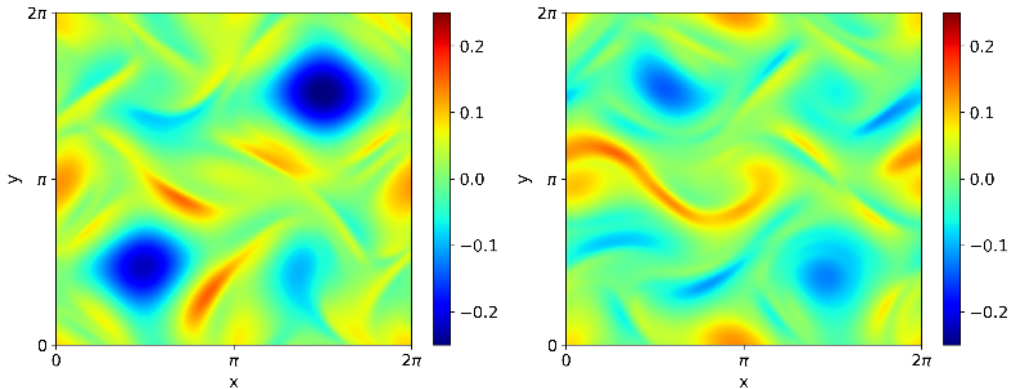
Fig. 4. Snapshot of the vorticity field for $Sc = 10^3$ at $t/T = 1200$ (left) and $t/T = 2212$ (right).
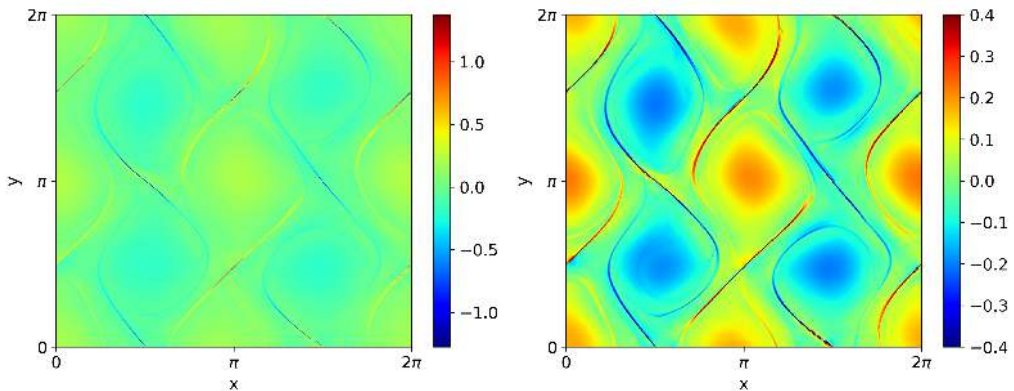

Fig. 5. Left: a representative snapshot of the vorticity field for $Sc = \infty$. Right: the same snapshot as in the left panel but with a rescaled colour bar. The purpose of this rescaling is to show the cellular structure of the flow more clearly.

stresses at the boundaries of the cells; inside the cells, the external force dominates and imposes the cellular structure. However, when polymer-stress diffusion becomes relevant (i.e. $Sc = 10^3$ and, with our choice of parameters, $Pe = 10^3$), large polymer stresses spread far from the straining lines where they are created and reach the interior of the vortices; this destabilizes the cellular structure and generates the symmetry breaking observed at $Sc = 10^3$. Furthermore, we note that although for $Sc = \infty$ polymers can locally be highly stretched (figure 6), the average polymer stretching is generally higher for $Sc = 10^3$ than for $Sc = \infty$ (figure 3).

Hameduddin *et al.* (2018) recently proposed to quantify the deviation of the polymer configuration from the equilibrium one by considering the geodesic distance between **C** and **I** in the space of positive-definite tensors. The snapshots of this distance (see the supplementary material) confirm the behaviours observed in the snapshots of tr **C** (figure 6).

Figures 4 and 5 also indicate that the vorticity field is much smoother for $Sc = 10^3$ than for $Sc = \infty$. This can be understood by noting that, in elastic turbulence, the small scales of the flow are not activated by a cascade phenomenon but rather by the fluctuations of the polymer feedback at the same scales, and for $Sc = 10^3$ the high-wave-number fluctuations of the polymer stress are damped by diffusivity. The smoothness of
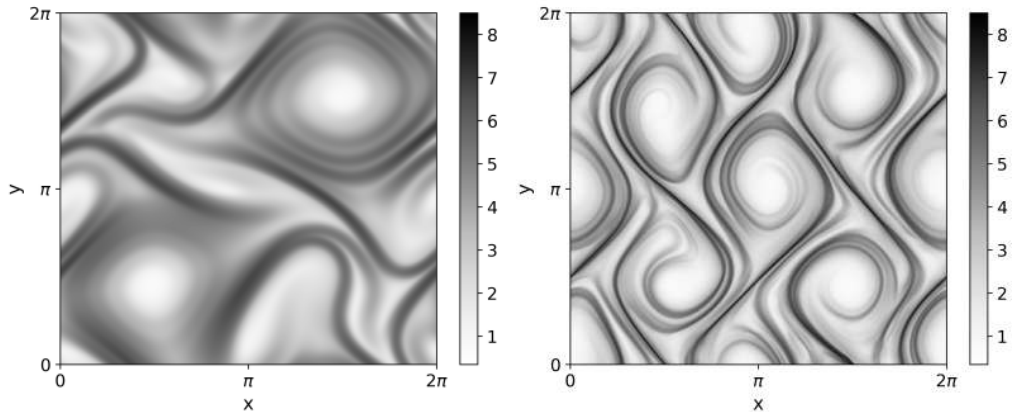
Fig. 6. Snapshots of $\ln(\mathrm{tr}\,\boldsymbol{C})$ for $Sc = 10^3$ (left) and $Sc = \infty$ (right). The snapshots are taken at the same times as in the left panel of figure 4 and in figure 5, respectively.
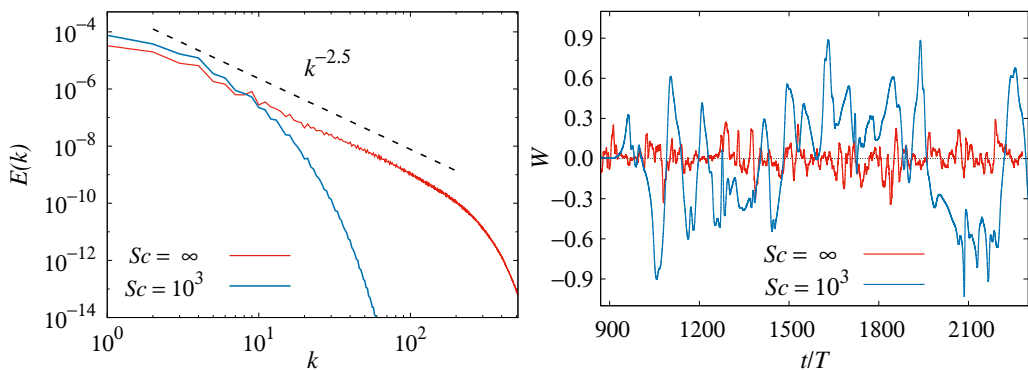

Fig. 7. Left: Kinetic-energy spectrum for $Sc = 10^3$ and $Sc = \infty$. For $Sc = \infty$ the spectrum behaves as the power-law $k^{-2.5}$. Right: Time series of W. For $Sc = 10^3$, W displays much larger fluctuations than for $Sc = \infty$.

the flow can be quantified by examining the spectrum of the velocity fluctuations, $E(k) \equiv \sum_{k-1/2 < k' \leqslant k+1/2} \langle |\hat{\boldsymbol{v}}(\boldsymbol{k}',t)|^2 \rangle_t$, where $\langle \cdot \rangle_t$ denotes the time average over the steady state and $\hat{\boldsymbol{v}}(\boldsymbol{k},t)$ is the Fourier transform of the velocity field minus its time average. We find again that artificial diffusivity has a strong impact on the flow (figure 7, left). For $Sc = 10^3$, $E(k)$ decay very rapidly with the wave number, whereas for $Sc = \infty$ it behaves as a power law: $E(k) \propto k^{-2.5}$. Thus, fluctuations are sustained at much smaller scales when $Sc = \infty$. The power law is shallower than those found previously in experiments and numerical simulations with different forcings, in which the exponent varied with the setup but was always smaller than -3 (Groisman & Steinberg 2000, 2004; Berti et al. 2008; Ray & Vincenzi 2016; Watanabe & Gotoh 2013, 2014; Gupta & Pandit 2017). A kinetic-energy spectrum steeper than k^{-3} was also predicted by Fouxon & Lebedev (2003). This prediction, however, does not necessarily apply to the case under consideration, because it assumes statistical homogeneity and isotropy and our flow does not enjoy these statistical symmetries. (Note that, for the Kolmogorov force, the same integration scheme used here yields the exponent -3.7 (Plan et al. 2017), which agrees with the results of Berti et al. (2008); see also Berti & Boffetta (2010) and Garg et al. (2018).)

To quantify the breaking of the cellular symmetry, we also consider the ratio

$$W = \frac{\omega(0,0) - \omega(\pi,0)}{\omega(0,0) + \omega(\pi,0)}, \tag{3.1}$$

which compares the amplitude of vorticity at two positions in the flow, $(x,y) = (0,0)$ and $(x,y) = (\pi,0)$. For the laminar solution ($\mu = 0$), these two positions are the centres of two equal-sign vortices and $W = 0$. Nonzero values of W therefore correspond to deviations from the cellular symmetry. Figure 7 (right) shows that the fluctuations of W are much bigger for $Sc = 10^3$ than for $Sc = \infty$ (analogous results are found for other couples of equal-sign vortices). This confirms that the cellular structure is strongly modified by artificial diffusivity.

4. Conclusions

In numerical simulations of constitutive models of polymer solutions the addition of artificial diffusivity is a well-known strategy for overcoming the numerical instabilities generated by the loss of positive definiteness of the polymer-stress tensor. We have studied the accuracy of this approach in elastic turbulence by comparing simulations of the two-dimensional Oldroyd-B model sustained by a cellular external force, with and without artificial diffusivity. Our results show that artificial diffusivity has a strong impact on the qualitative spatial and temporal properties of the flow. In particular, with artificial diffusivity the cellular structure imposed by the external force breaks down, as also found by Thomases & Shelley (2009) and Thomases *et al.* (2011) for a four-roll mill force and the same value of Sc. Without artificial diffusivity, the flow is mainly perturbed in strain-dominated regions but, albeit chaotic, essentially reproduces the symmetries of the background force.

We have also performed simulations of the FENE-P model in exactly the same setting and found similar results (see Appendix A); hence the effect of artificial diffusivity is not modified by the nonlinearity of the elastic force.

To preserve the positive definiteness of the polymer conformation tensor and accurately resolve its gradient, we have used a combination of the Cholesky decomposition and the Kurganov–Tadmor hyperbolic solver. Adding artificial diffusivity to this scheme produces the migration of high polymer stresses to regions of the flow where in principle polymers would be weakly stretched. This generates strong differences in the large-scale flow. We believe that this effect of artificial diffusivity is not specific to the Kurganov–Tadmor scheme, i.e. the addition of an excessively large polymer-stress diffusion is expected to produce analogous modifications of the large-scale flow also in other integration schemes and, vice versa, if a scheme does not use artificial diffusivity or similar dissipation terms, it should not produce the symmetry breaking discussed above.

We have described the motion of the fluid by means of the Stokes equations, as in some of the previous studies on elastic turbulence. Other studies have used the Navier–Stokes equations. Thus, we have also performed numerical simulations of $(2.1b)$ coupled with the Navier–Stokes equations with the same cellular force. The Reynolds number $Re = f_0/\nu^2 K^3$ has been set to unity, which is below the critical value for the appearance of inertial instabilities, $Re_c = \sqrt{2}$ (Gotoh & Yamada 1984). The conclusions on the effect of artificial diffusivity are exactly the same as when the Stokes equations are used.

In our study, we specifically selected the cellular force in order to illustrate the impact of artificial diffusivity on numerical simulations of elastic turbulence. This force indeed generates a flow in which the straining and vortical regions are distinct. Hence in the absence of artificial diffusivity the polymer stress is chiefly located at the straining regions,

whereas in the presence of diffusivity it spreads outside them. For other external forces that mix strain and vorticity, the effect of artificial diffusivity may be less dramatic. This is the case, for instance, of the Kolmogorov force, which in the absence of polymer feedback and at low Reynolds numbers generates a sinusoidal shear. For the Kolmogorov force, the velocity spectrum indeed behaves as a power law even for $Sc = 10^3$ (Garg *et al.* 2018), although of course the power law is observed on a smaller range of wave numbers compared to simulations that do not use artificial diffusivity (Plan *et al.* 2017).

The effect of artificial diffusivity is more dramatic in elastic turbulence than at high Reynolds numbers or in laminar flows. In these latter cases, indeed, artificial diffusivity produces quantitative changes in the solution of the Oldroyd-B and FENE-P models but does not modify the qualitative behaviour of the velocity and polymer-conformation fields, provided of course Sc is not excessively small (see, e.g., figures 8 to 10 in Vaithianathan *et al.* 2006 and figures 3 and 4 in Sid *et al.* 2018 for the high-Reynolds-number regime and figure 7 in Thomases 2011 for the laminar regime). In elastic turbulence, before the addition of polymers the flow is laminar. Artificial diffusivity thus strongly modifies the large-scale flow by bringing high polymer stresses to regions of the fluid where the polymers would be weakly stretched and hence the flow would be weakly chaotic. This effect is peculiar to the regime of elastic turbulence and can lead to the spurious behaviours described above. Therefore, great caution should be taken in using artificial diffusivity to prevent numerical instabilities in simulations of elastic turbulence.

Appendix A. Effect of artificial diffusivity in the FENE-P model

A drawback of the Oldroyd-B model is that there is not a maximum polymer extension. Infinitely large extensions are in principle allowed, and in certain flow conditions tr $\boldsymbol{C}$ grows indefinitely. In the FENE-P model, a maximum polymer extension $\ell_{\max}$ is imposed by modifying (2.1) as follows

$$\boldsymbol{\nabla} p = \nu \Delta \boldsymbol{u} + \frac{\mu}{\tau} \boldsymbol{\nabla} \cdot [h(\mathrm{tr}\,\boldsymbol{C})\boldsymbol{C}] + \boldsymbol{f}, \qquad \boldsymbol{\nabla} \cdot \boldsymbol{u} = 0, \qquad (A\,1a)$$

$$\partial_t \boldsymbol{C} + \boldsymbol{u} \cdot \boldsymbol{\nabla} \boldsymbol{C} = (\boldsymbol{\nabla} \boldsymbol{u}) \cdot \boldsymbol{C} + \boldsymbol{C} \cdot (\boldsymbol{\nabla} \boldsymbol{u})^\top - \frac{h(\mathrm{tr}\,\boldsymbol{C})\boldsymbol{C} - \boldsymbol{I}}{\tau}, \qquad (A\,1b)$$

where

$$h(\zeta) = \frac{\ell_{\max}^2 - 2}{\ell_{\max}^2 - \zeta}. \qquad (A\,2)$$

The function $h(\mathrm{tr}\,\boldsymbol{C})$ diverges as tr $\boldsymbol{C}$ approaches $\ell_{\max}^2$ and hence causes tr $\boldsymbol{C}$ to stay smaller than $\ell_{\max}^2$.

In this Appendix, we report simulations of the FENE-P model with and without artificial diffusion. The maximum polymer square extension is $\ell_{\max}^2 = 3 \times 10^3$, while the other parameters of the FENE-P model are the same as those used for the Oldroyd-B model in § 3. Equation (A 1b) is solved by combining the Cholesky decomposition and the Kurganov-Tadmor hyperbolic solver as described in § 2. The effect of artificial diffusivity is once again studied by adding the term $\kappa \Delta \boldsymbol{C}$ with $\kappa = 5 \times 10^{-5}$ to (A 1b), so that $Sc = 10^3$. Figures 8 and 9 are the counterparts for the FENE-P model of figures 2 (right panel), 6 and 7 (left panel). The results show that the conclusions on the effects of
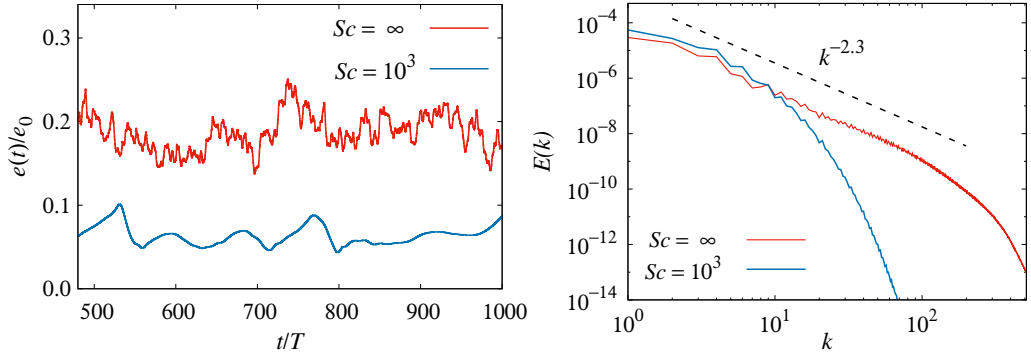
Fig. 8. FENE-P model. Left: Time series of the rescaled kinetic energy in the steady state for $Sc = \infty$ (red, top curve) and $Sc = 10^3$ (blue, bottom curve). Right: Kinetic-energy spectra for $Sc = 10^3$ and $Sc = \infty$. For $Sc = \infty$ the spectrum behaves as the power-law $k^{-2.3}$.
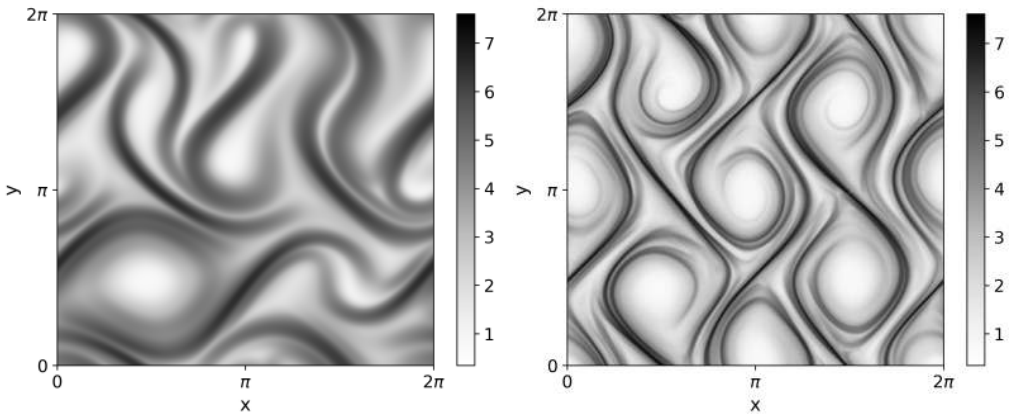

Fig. 9. FENE-P model: Representative snapshots of $\ln(\text{tr } \boldsymbol{C})$ in the steady state for $Sc = 10^3$ (left) and $Sc = \infty$ (right).

artificial diffusivity obtained for the Oldroyd-B model hold analogously for the FENE-P model.

ABED, W. M., WHALLEY, R. D., DENNIS, D. J. C. & POOLE R. J. 2016 Experimental investigation of the impact of elastic turbulence on heat transfer in a serpentine channel. *J. Non-Newtonian Fluid Mech.* **231**, 68–78.

BALCI, N., THOMASES, B., RENARDY, M. & DOERING, C. R. 2011 Symmetric factorization of the conformation tensor in viscoelastic fluid models. *J. Non-Newtonian Fluid Mech.* **166**, 546–553.

BERTI, S., BISTAGNINO, A., BOFFETTA, G., CELANI, A. & MUSACCHIO, S. 2008 Two-dimensional elastic turbulence. *Phys. Rev.* E **77**, 055306(R).

BERTI, S. & BOFFETTA, G. 2010 Elastic waves and transition to elastic turbulence in a two-dimensional viscoelastic Kolmogorov flow. *Phys. Rev.* E **82**, 036314.

BIRD, R. B., HASSAGER, O., ARMSTRONG, R. C. & CURTISS, C. F. 1987 *Dynamics of Polymeric Liquids*, vol. II. Wiley.

VAN BUEL, R., SCHAAF, C. & STARK, H. 2018 Elastic turbulence in two-dimensional Taylor-Couette flows. *Europhys. Lett.* **124**, 14001.

CARDOSO, O., MARTEAU, D. & TABELING, P. 1994 Quantitative experimental study of the free decay of quasi-two-dimensional turbulence. *Phys. Rev. E* **49**, 454–461.

DALLAS, V., VASSILICOS, J. C. & HEWITT, G. F. 2010 Strong polymer-turbulence interactions in viscoelastic turbulent channel flow. *Phys. Rev. E* **82**, 066303.

EL-KAREH, A. W. & LEAL, L. G. 1989 Existence of solutions for all Deborah numbers for a non- Newtonian model modified to include diffusion. *J. Non-Newtonian Fluid Mech.* **33**, 257–287.

FATTAL, R. & KUPFERMAN, R. 2004 Constitutive laws for the matrix-logarithm of the conformation tensor. *J. Non-Newtonian Fluid Mech.* **123**, 281–285.

FOUXON, A. & LEBEDEV, V. 2003 Spectra of turbulence in dilute polymer solutions. *Phys. Fluids* **15**, 2060–2072.

GARG, H., CALZAVARINI, E., MOMPEAN, G. & BERTI, S. 2018 Particle-laden two-dimensional elastic turbulence, *Eur. Phys. J. E* **41**, 115.

GOTOH, K. & YAMADA, M. 1984 Instability of a cellular flow. *J. Phys. Soc. Japan* **53**, 3395–3398.

GRAHAM, M. D. 2014 Drag reduction and the dynamics of turbulence in simple and complex fluids. *Phys. Fluids* **26**, 101301.

GROISMAN, A. & STEINBERG, V. 2000 Elastic turbulence in a polymer solution flow. *Nature* **405**, 53–55.

GROISMAN, A. & STEINBERG, V. 2001 Efficient mixing at low Reynolds numbers using polymer additives. *Nature* **410**, 905–908.

GROISMAN, A. & STEINBERG, V. 2004 Elastic turbulence in curvilinear flows of polymer solutions. *New J. Phys.* **6**, 29.

GRILLI, M., VÁZQUEZ-QUESADA, A. & ELLERO, M. 2013 Transition to turbulence and mixing in a viscoelastic fluid flowing inside a channel with a periodic array of cylindrical obstacles. *Phys. Rev. Lett.* **110**, 174501.

GUPTA, A. & PANDIT, R. 2017 Melting of a nonequilibrium vortex crystal in a fluid film with polymers: Elastic versus fluid turbulence. *Phys. Rev. E* **95**, 033119.

GUPTA, A., PERLEKAR, P. AND PANDIT, R. 2015 Two-dimensional homogeneous isotropic fluid turbulence with polymer additives. *Phys. Rev. E* **91**, 033013.

HAMEDUDDIN, I., MENEVEAU, C., ZAKI, T. A. & GAYME, D. F. (2018) Geometric decomposition of the conformation tensor in viscoelastic turbulence. *J. Fluid Mech.* **842**, 395–427.

JIN, S. & COLLINS, L. R. 2007 Dynamics of dissolved polymer chains in isotropic turbulence. *New J. Phys.* **9**, 360.

JOSEPH, D. D. 1990 *Fluid dynamics of viscoelastic liquids.* Springer.

KURGANOV, A. & TADMOR, E. 2000 New high-resolution central schemes for nonlinear conservation laws and convection-diffusion equations. *J. Comput. Phys.* **160**, 241–282.

LIU N. & KHOMAMI, B. 2013 Elastically induced turbulence in Taylor–Couette flow: direct numerical simulation and mechanistic insight *J. Fluid Mech.* **737**, R4.

LIU, Y. & STEINBERG, V. 2014 Single polymer dynamics in a random flow. *Macromol. Symp.* **337**, 34–43.

MIN, T., YOO, J. Y. & CHOI, H. 2001 Effect of spatial discretization schemes on numerical solutions of viscoelastic fluid flows. *J. Non-Newtonian Fluid Mech.* **100**, 27–47.

OLDROYD, J. G. 1950 On the formulation of rheological equations of state. *Proc. R. Soc. Lond. A* **200**, 523–541.

PERLEKAR, P., MITRA, D. & PANDIT, R. 2006 Manifestations of drag reduction by polymer additives in decaying, homogeneous, isotropic turbulence. *Phys. Rev. Lett.* **97**, 264501.

PERLEKAR, P., MITRA, D. & PANDIT, R. 2010 Direct numerical simulations of statistically steady, homogeneous, isotropic fluid turbulence with polymer additives. *Phys. Rev. E* **82**, 066313.

PLAN, E. L. C. VI M., GUPTA, A., VINCENZI, D. & GIBBON, J. D. 2017 Lyapunov dimension of elastic turbulence. *J. Fluid Mech.* **822**, R4.

POOLE, R. J., BUDHIRAJA, B., CAIN, A. R. & SCOTT, P. A. 2012 Emulsification using elastic turbulence. *J. Non-Newtonian Fluid Mech.* **177–178**, 15–18.

PRESS, W. H., TEUKOLSKY, S. A., VETTERLING, W. T & FLANNERY, B. P. 2007 *Numerical recipes: The art of scientific computing*, 3rd edition. Cambridge University.

RAY, S. S. & VINCENZI, D. 2016 Elastic turbulence in a shell model of polymer solution. *Europhys. Lett.* **114**, 44001.

ROBERT, A., VAITHIANATHAN, T., COLLINS, L. R. & BRASSEUR, J. G. 2010 Polymer-laden homogeneous shear-driven turbulent flow: a model for polymer drag reduction. *J. Fluid Mech.* **657**, 189–226.

ROTHSTEIN, D., HENRY, E. & GOLLUB, J. P. 1999 Persistent patterns in transient chaotic fluid mixing. *Nature* **401**, 770–772.

SID, S., TERRAPON, V. E. & DUBIEF, Y. 2018 Two-dimensional dynamics of elasto-inertial turbulence and its role in polymer drag reduction. *Phys. Rev. Fluids* **3**, 011301(R).

SHEKAR, A., MCMULLEN, R. M., WANG, S.–N., MCKEON, B. J. & GRAHAM, M. D. (2018) Critical layer structures and mechanisms in elastoinertial turbulence. `arXiv:1811.00524`.

SURESHKUMAR, R. & BERIS, A. N. 1995 Effect of artificial stress diffusivity on the stability of numerical calculations and the flow dynamics of time-dependent viscoelastic flows. *J. Non-Newtonian Fluid Mech.* **60**, 53–80.

THOMASES, B. & SHELLEY, M. 2009 Transition to mixing and oscillations in a Stokesian viscoelastic flow. *Phys. Rev. Lett.* **103**, 094501.

THOMASES, B., SHELLEY, M. & THIFFEAULT, J.-L. 2011 A Stokesian viscoelastic flow: Transition to oscillations and mixing. *Physica* D **240**, 1602–1614.

THOMASES, B. 2011 An analysis of the effect of stress diffusion on the dynamics of creeping viscoelastic flow. *J. Non-Newtonian Fluid Mech.* **166**, 1221–1228.

TRAORE, B., CASTELAIN, C. & BURGHELEA, T. 2015 Efficient heat transfer in a regime of elastic turbulence. *J. Non-Newtonian Fluid Mech.* **223**, 62–76.

VAITHIANATHAN, T. & COLLINS, L. R. 2003 Numerical approach to simulating turbulent flow of a viscoelastic polymer solution. *J. Comp. Phys.* **187**, 1–21.

VAITHIANATHAN, T., ROBERT, A., BRASSEUR, J. G. & COLLINS, L. R. 2006 An improved algorithm for simulating three-dimensional, viscoelastic turbulence. *J. Non-Newtonian Fluid Mech.* **140**, 3–22.

VAITHIANATHAN, T., ROBERT, A., BRASSEUR, J. G. & COLLINS, L. R. 2007 Polymer mixing in shear-driven turbulence. *J. Fluid Mech.* **585**, 487–497.

VALENTE P. C., DA SILVA, C. B. & PINHO, F. T. 2014 The effect of viscoelasticity on the turbulent kinetic energy cascade. *J. Fluid Mech.* **760**, 39–62.

WATANABE, T. & GOTOH, T. 2013 Kinetic energy spectrum of low-Reynolds-number turbulence with polymer additives. *J. Phys. Conf. Ser.* **454**, 012007.

WATANABE, T. & GOTOH, T. 2014 Power-law spectra formed by stretching polymers in decaying isotropic turbulence. *Phys. Fluids* **26**, 035110.

Effect of polymer-stress diffusion in the numerical simulation of elastic turbulence

SUPPLEMENTARY MATERIAL

Anupam Gupta[1] and Dario Vincenzi[2]

[1]Paulson School of Engineering and Applied Sciences, Harvard University, Cambridge, Massachusetts 02138, USA

[2]Université Côte d'Azur, CNRS, LJAD, 06100 Nice, France

This supplementary material consists of additional simulations of the Oldroyd-B model on the periodic square $[0, 2\pi]^2$ with a cellular forcing (see (2.1) and (2.2) in the main text). The integration method is described in § 2 of the manuscript.

Figures 1 and 2 are the analogues of figures 2 (right panel), 6 and 8 (left panel) in the main text for $\tau = 40$, $\mu = 0.02$ and same K, f_0, ν as in § 2. In particular, the Deborah number is now $De = 8$ and the coupling coefficient μ is doubled.

Figures 3 and 4 are the analogues of figures 2 (right panel), 6 and 8 (left panel) in the main text for $K = 4$, $\tau = 10$, $f_0 = 0.16$ and same ν and μ as in § 2. The Deborah number is $De = 8$ and the spatial frequency of the forcing is doubled compared to the main text.

These additional simulations support the validity of the conclusions reported in the manuscript.

Finally, figure 5 shows the quantity $d^2(\mathbf{I}, \mathbf{C}) = \mathrm{tr} \log^2(\mathbf{C})$, which represents the geodesic distance between the conformation tensor and the identity tensor in the space of positive-definite tensors [see Hameduddin *et al.*, *J. Fluid Mech.* **842**, 395 (2018)] for the same parameters as in § 3 of the main text.
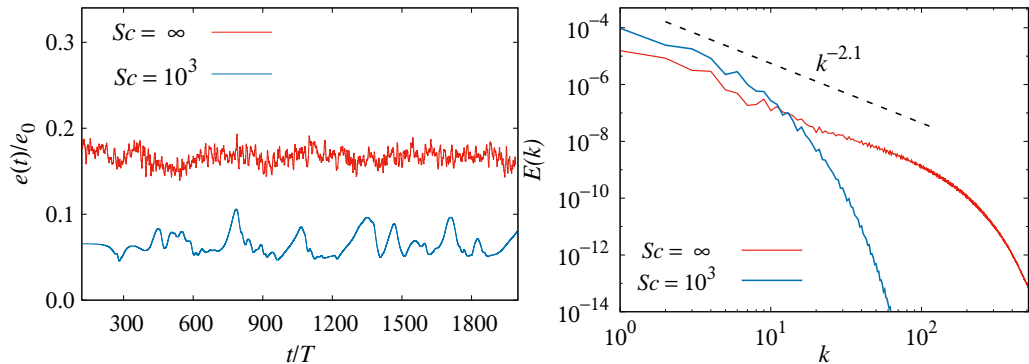
Fig. 1. Time series of the rescaled kinetic energy in the steady state (left) and kinetic-energy spectra (right) for the Oldroyd-B model with $\nu = 0.05$, $f_0 = 0.02$, $K = 2$, $De = 8$, $\mu = 0.02$.
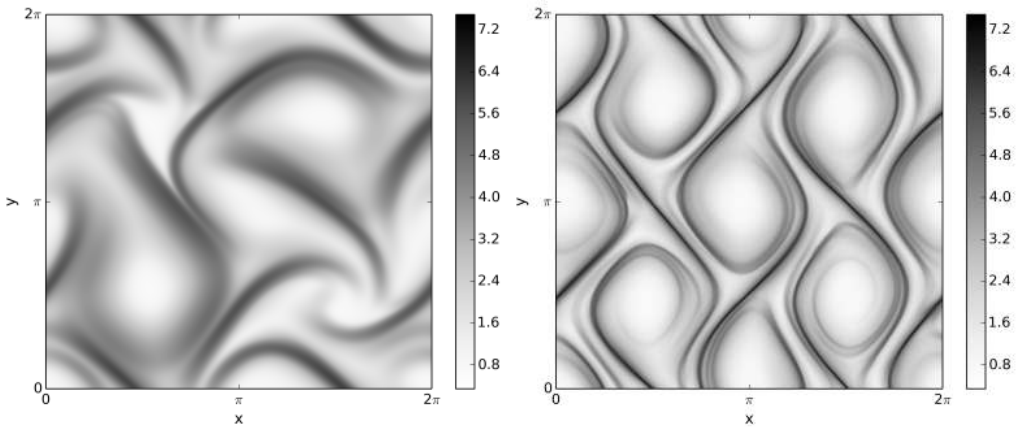

Fig. 2. Representative snapshots of $\ln(\mathrm{tr}\,\boldsymbol{C})$ in the steady state for the Oldroyd-B model with $\nu = 0.05$, $f_0 = 0.02$, $K = 2$, $De = 8$, $\mu = 0.02$ and $Sc = 10^3$ (left) and $Sc = \infty$ (right).
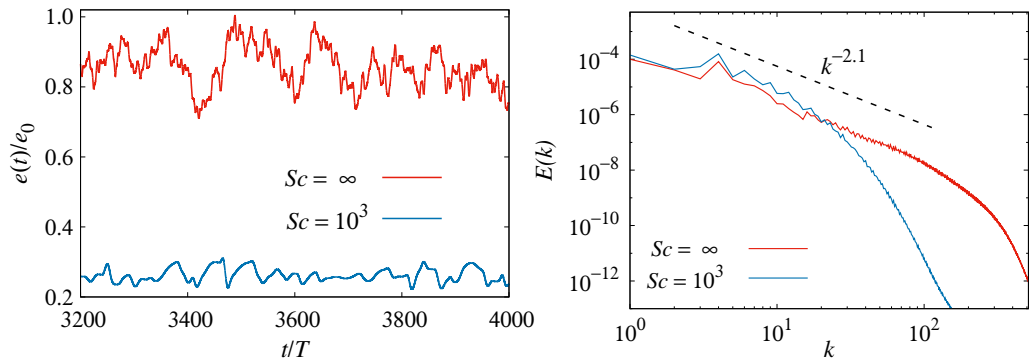
Fig. 3. Time series of the rescaled kinetic energy in the steady state (left) and kinetic-energy spectra (right) for the Oldroyd-B model with $\nu = 0.05$, $f_0 = 0.16$, $K = 4$, $De = 8$, $\mu = 0.01$.
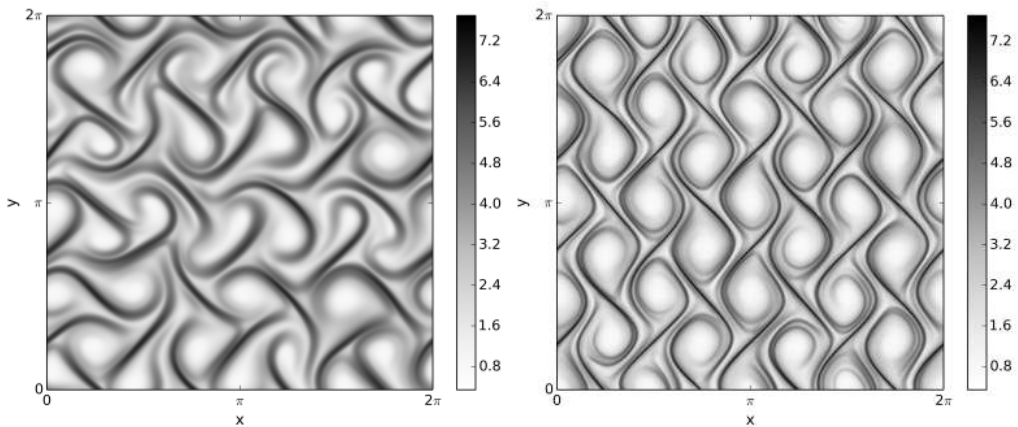

Fig. 4. Representative snapshots of $\ln(\mathrm{tr}\, \boldsymbol{C})$ in the steady state for the Oldroyd-B model with $\nu = 0.05$, $f_0 = 0.16$, $K = 4$, $De = 8$, $\mu = 0.01$ and $Sc = 10^3$ (left) and $Sc = \infty$ (right).
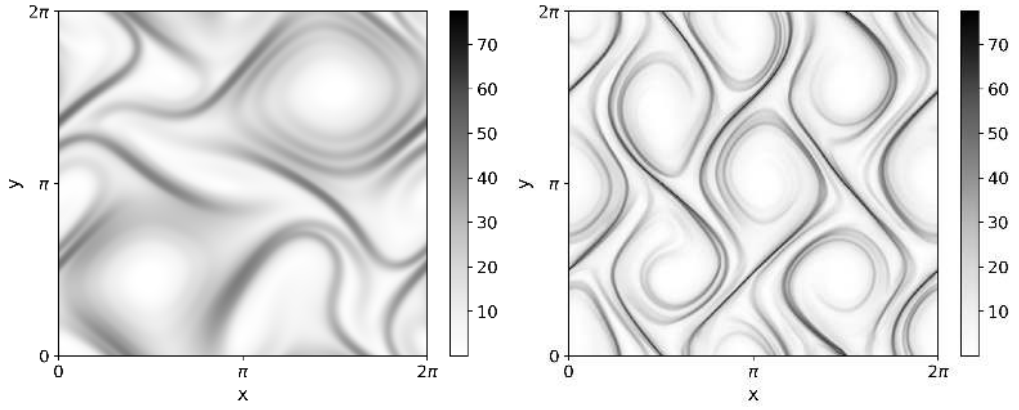
Fig. 5. Snapshots of $d^2(\mathbf{I}, \mathbf{C})$ for $Sc = 10^3$ (left) and $Sc = \infty$ (right) and the same parameters and time instants as in figure 6 of the main text.